Supporting Information for

Label-free single nanoparticle identification and characterization in demanding environment, including infectious emergent virus

Minh-Chau Nguyen [1,*], Peter Bonnaud [1], Rayane Dibsy [2], Guillaume Maucort [3], Sébastien Lyonnais [4], Delphine Muriaux [2,4], Pierre Bon [1,*]

*corresponding authors : minh-chau.nguyen@cnrs.fr, pierre.bon@cnrs.fr

Table of contents

Other Supplementary Materials for this manuscript include the following:
Movies S1 to S4

S1 3D reconstruction from 2D images

Intensity and phase images allow to generate a scalar electromagnetic field at the imaging plane $\mathrm{I}_{z_0} = A_0^2 \exp(i\,\varphi_{z_0})$. Because the system is illuminated by a coherent source, the electromagnetic field can be propagated to different planes by a factor of $\exp(i\,k_z\,\Delta z)$, where k_z is the wave vector in axial direction, Δz is the distance to the imaging plane.

Finally, intensity and phase image at different planes are determined by the convolution of electromagnetic field and the back focal plane images H_{BLP}, represented as Ewald's sphere [1, 2].

$$
\begin{aligned}
& E(\Delta z) = I(\Delta z) * H_{BLP}(\Delta z) = [I_0\ \exp(i\,k_z\,\Delta z)] * H_{BLP}(\Delta z) \\
\Rightarrow\ & E(\Delta z) = \mathcal{F}^{-1}\left[\mathcal{F}\left(I_0\ \exp(i\,k_z\,\Delta z)\right) \cdot \mathcal{F}\left(H_{BLP}(\Delta z)\right)\right] \\
\Rightarrow\ & A(\Delta z) = ||\mathrm{E}(\Delta z)|| \quad \text{and} \quad \varphi(\Delta z) = \angle \mathrm{E}(\Delta z).
\end{aligned}
$$

S2 Explicit expression of Rytov intensity

While a light beam $I_0 = A_0^2 \exp(i\varphi_0)$ passes through a medium (in our case, the solution of NP), the background electromagnetic field is:

$$I_{bkg} = A_0^2 \exp\left[i\left(\varphi_0 + \frac{2\pi}{\lambda}(n_m + i\,n'_m)\int dz\right)\right] \tag{S1}$$

, where $n_m + i\,n'_m$ the medium complex refractive index.

If a NP is present along the optical path and the diffraction is neglected, the electromagnetic field is affected by the complex refractive index $n + i\,n'$ of the NP and can be written as:

$$I = A_0 \exp\left[i\left(\varphi_0 + \frac{2\pi}{\lambda}(n + i\,n')\int dz\right)\right]. \tag{S2}$$

Our detection method represents the ratio between the light passed through the NP and the background which is expressed from the equation (S2) and (S1):

$$t = \frac{I}{I_{bkg}} = \underbrace{\exp\left(-\frac{2\pi}{\lambda}(n' - n'_m)\int dz\right)}_{\sqrt{T}\,:\,\text{transmissivity}} \exp\left[i\,\frac{2\pi}{\lambda}\underbrace{(n - n_m)\int dz}_{\Delta\ell\,:\,\text{optical path difference (OPD)}}\right]. \tag{S3}$$

Images of INT and OPD are therefore expressed :

$$\begin{cases} \textbf{INT image :}\ T = \left\|\dfrac{I}{I'}\right\| = \exp\left(-\frac{2\pi}{\lambda}(n' - n'_m)\int dz\right) \\ \textbf{OPD image:}\ \Delta\ell = (n - n_m)\int dz \end{cases}. \tag{S4}$$

In this paper, we use a complex observable, called Rytov's field, to combine the intensity I and the optical path difference $\Delta\ell$:

$$E_{Rytov} = \frac{i\lambda n_m}{\pi}\left[\ln\sqrt{T} + i\,\frac{2\pi}{\lambda}\Delta\ell\right]. \tag{S5}$$

Various researches reported that the surface integration of phase image enables the characterization of samples [3, 4]. Here, we also introduce a surface integration of Rytov field (SIR), which is expressed below by using (S4) :

$$\begin{aligned} \text{SIR} &= \iint E_{Rytov}\,dx\,dy = \sum_X\sum_Y \frac{i\lambda n_m}{\pi}\delta_{px}^2\left[\ln\sqrt{T} + i\,\frac{2\pi}{\lambda}\Delta\ell\right] \\ &= \sum_X\sum_Y \frac{i\lambda n_m}{\pi}\delta_{px}^2\left[-\frac{\pi}{\lambda}(n' - n'_m)\int dz + i\frac{2\pi}{\lambda}(n - n_m)\int dz\right] \\ &= \left(\underbrace{\sum_X\sum_Y -2n_m\,\delta_{px}^2\,(n - n_m)\int dz}_{\text{Re(SIR)}}\right) + i\left(\underbrace{\sum_X\sum_Y -n_m\,\delta_{px}^2\,(n' - n'_m)\int dz}_{\text{Im(SIR)}}\right). \end{aligned} \tag{S6}$$

Here δ_{px} is the pixel size at object plane. The sum of all the pixel $\sum_X \sum_Y \delta_{px}^2 \int dz$ can be converted to the volume integration $\iiint dx\, dy\, dz = \gamma \cdot V_{obj}$, which is proportional to the NP's volume by a factor γ. Theoretically, a whole–surface integration represent a factor $\gamma = 1$, but in practice, our surface integration is realized within the first bright ring of image. The coefficient $\gamma = 0.77$ is determined by using Product-Of-Convolution simulation [5, 6], in order to maximize the signal to noise ratio.

Consequently, SIR intensity (real and imaginary part) is related to the complex refractive indices of particle and medium, as well as the NP volume. Each of these properties can be extracted if others are known.

• Determination of NP mass

When there is no resonance emerging from the shape and size of the particle (such as for dielectric particles), the bulk material refractive index is a precise approximation to describe the NP refractive index. We can therefore derived the NP mass from:

$$\begin{aligned}
\mathrm{SIR} &= -2n_m \iint \Delta\ell \cdot dx\, dy + i\left(-n_m\,(n' - n'_m) \iint dx\, dy \int dz\right) \\
&= -2n_m\,(n - n_m) \iiint dx\, dy\, dz + i\left(-n_m\,(n' - n'_m) \iiint dx\, dy\, dz\right) \\
&= -\frac{2n_m\,(n - n_m)}{\rho_{obj}}\,\gamma \underbrace{\rho_{obj}\, V_{obj}}_{\text{m : NP mass}} + i\left(-\frac{n_m\,(n' - n'_m)}{\rho_{obj}}\,\gamma \underbrace{\rho_{obj}\, V_{obj}}_{\text{m : NP mass}}\right).
\end{aligned} \tag{S7}$$

From (S6) and (S7), our values of Re(SIR) and Im(SIR) are both proportional to the NP mass.

$$m = -\underbrace{\frac{\rho_{obj}}{2\,\gamma\, n_m\,(n - n_m)}}_{\beta_{SIR}} \cdot \mathrm{Re(SIR)} = -\beta_{SIR} \cdot\ \mathrm{Re(SIR)}, \tag{S8}$$

$$m = -\underbrace{\frac{\rho_{obj}}{\gamma\, n_m\,(n' - n'_m)}}_{\beta'_{SIR}} \cdot \mathrm{Im(SIR)} = -\beta'_{SIR} \cdot\ \mathrm{Im(SIR)}. \tag{S9}$$

In our case, the dielectric particles and the solution are mostly transparent ($n' \approx 0$ and $n'_m \approx 0$). Therefore, the calculation of mass is carried out by the real part of SIR.

• Determination of complex refractive index

For metal NP, refractive index can be drastically changed from their bulk value due to surface plasmon effect. For homogeneous spherical particles, we can calculate NP mass, knowing the density and NP size d, SIR intensity enables a method of complex refractive index determination.

Equations (S8) and (S9) are re-written allowing to derive the refractive index.

$$n = n_m + \frac{\rho_{obj}}{2\,\gamma\, n_m} \cdot \frac{\mathrm{Re(SIR)}}{m} = n_m + \frac{3\,\mathrm{Re(SIR)}}{\gamma\, n_m\, \pi\, d^3}, \tag{S10}$$

$$n' = n'_m + \frac{\rho_{obj}}{\gamma\, n_m} \cdot \frac{\mathrm{Im(SIR)}}{m} = n'_m + \frac{6\,\mathrm{Im(SIR)}}{\gamma\, n_m\, \pi\, d^3}. \tag{S11}$$

S3 System metrology

S3.1 Illumination characteristics

A white-light supercontinuum laser (ElectroVIS, Leukos, France) illuminates the sample. Its full spectrum is shown in Figure S1a. The illumination is filtered in order to agree certain criteria. The (spatial and temporal) coherence must be high enough so that the numerical propagation is still valid, but also low enough to limit the emergence of speckle pattern.
- The illumination is filtered by a bandpass filter (Thorlabs FBH450-10, 450nm, FWHM = 10nm).
- Numerical aperture (NA) of the illumination is $\mathrm{NA}_{ill} = 0.024$, measured at back focal plane. It is about 2% of the collection NA ($\mathrm{NA}_{coll} = 1.3$).

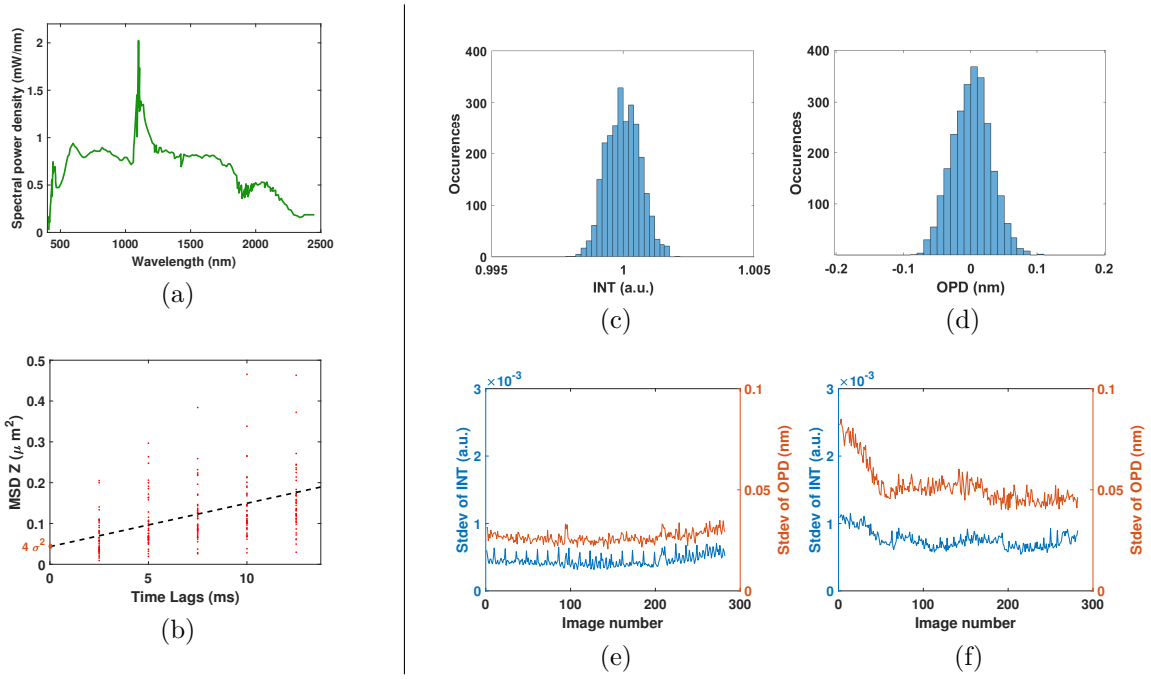

Figure S1: **Characteristics of system.(a)** Full spectrum of supercontinuum laser. **(b)** Example for localization precision of SARS-COV-2 in Z-direction. **(c, d)** Histogram of INT (c) and OPD (d) of an image. **(e, f)** Standard deviation of INT and OPD for all the acquisition without any sample (e) and with a sample of pure water (f).

S3.2 Localization precision

Here, we discuss about our localization precision of moving nanoparticles. To consider the worst and honest scenario, the localization precision of SARS-CoV-2 nanoparticles acquired under a biosafety cabinet is measured. The linear fit of the graph of mean squared displacement as function of time lags allows to estimate NP size as well as localization precision. Its slope is proportional to the diffusion coefficient, while its intercept is equal to $4\sigma^2$, where σ the localization precision [7]. The intercept is visualized as the ordinate at the origin, as show in Figure S1b.

In the case of SARS-CoV-2 virus, the localization precision is determined as **about 30nm on XY-direction and about 100nm on Z-direction**. The XY localization precision is below the statistical displacement of the virus within the exposure time (root mean square displacement of 90-nm in each direction during $t_{expo} = 0.9$ ms).

S3.3 Phase and Intensity signal-to-noise ratio

An acquisition of 282 images without any object was collected. The acquired images contains the intrinsic noise of the setup. The histograms of intensity (INT) and optical path difference (OPD) exhibits the spatial measurement precision (Fig. S1c and S1d). Figure S1e shows the standard deviation of all the images in the acquisition. The measurement precision is defined as the median value :

$$\sigma_{\mathrm{INT,s}} = 0.04\% \quad \text{and} \quad \sigma_{\mathrm{OPD,s}} = 0.026 \text{ nm} = 26 \text{ pm} \approx \frac{\lambda}{20000} .$$

In our case, because the experiment is carried out in solution, the measurement precision is evaluated by imaging a sample of ultra-pure water. Figure S1f shows the measurement precision of all the image. The measurement precision is defined as the median value :

$$\sigma_{\mathrm{INT,s}} = 0.07\% \quad \text{and} \quad \sigma_{\mathrm{OPD,s}} = 0.050 \text{ nm} = 50 \text{ pm} \approx \frac{\lambda}{10000} .$$

The difference between these two noise evaluation is attributed to the fluctuation of solution.

S4 Rytov analysis and Polarizability analysis

In the study of Khadir *et al.* [8], both intensity and phase images are used in order to derive the polarizability of the particle. Their equation is based on the expression of electromagnetic field, *i.e.* an exponentiation of phase shift. In this case, the real and imaginary part of refractive index contributed in the expressions of both real and imaginary part of polarizability, as shown in the following equation (from [8]).

$$\mathrm{Re}(\alpha) = \frac{\lambda_0\, n}{\pi} \iint \sqrt{(T(x,y))}\, \sin(k_0\, \delta\ell(x,y))\, dx\, dy$$

$$\mathrm{Im}(\alpha) = \frac{\lambda_0\, n}{\pi} \iint \left[1 - \sqrt{(T(x,y))}\, \cos(k_0\, \delta\ell(x,y))\right] dx\, dy$$

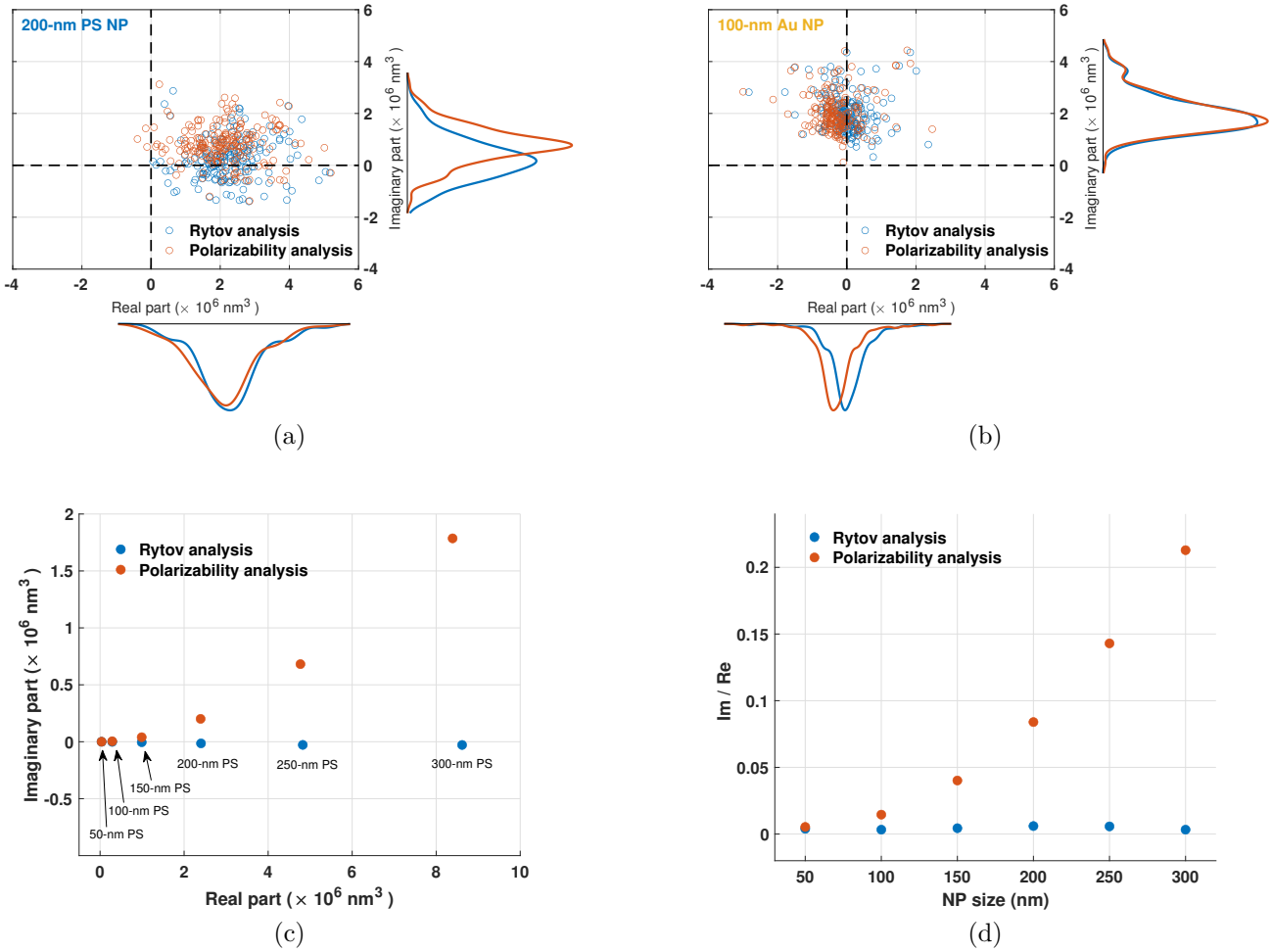

Figure S2: Comparison between our Rytov analysis (blue points and lines) and Polarizability analysis in the previous study of Khadir *et al.* (orange points and lines). Scatter graph of real and imaginary part(of Rytov field and polarizability respectively) **(a)**for 200-nm PS and **(b)** for 100-nm Au. **(c)** Variation of the imaginary part (of Rytov field and polarizability respectively) in function of NP size of PS NP. **(d)** Variation of the imaginary part (of Rytov field and polarizability respectively) in function of NP size of PS NP.

Comparing to their method, our Rytov intensity uses a logarithm of the electromagnetic field. It gives a better orthogonality between the real and imaginary part when computed to

extract the complex refractive index : the real (imaginary, respectively) part of Rytov field is proportional to the real (imaginary, respectively) of refractive index.

Figure S2 confirms our statement. Figure S2a describes the experimental results of 200-nm PS NP in both methods. For the convenience of comparison, the sign of Rytov field real part has been changed, since its value is negative, by our definition, in the equation S5. We remark that in water, for PS NP, the imaginary part of refractive index difference is is negligible when compared to the real part [9] since PS particles are dielectric objects.. As a result, in our Rytov analysis, the imaginary part is almost vanished, and the information can be derived from the real part. On the other hand, the imaginary part of polarizability is still important, and the retrieval of information must be done using both real and imaginary part. The same feature is obtained in the case of 100-nm Au NP, but for the real part (Fig S2b).

Using a simulation approach for PS NP, the variations of Rytov field and polarizability in function of NP size are represented in Fig. S2c and S2d. Although the imaginary part of polarizability varies exponentially with NP size, the imaginary part of Rytov field remains approximately to 0 for all simulated NP size (from 50 nm to 300 nm). Ratio between imaginary and real part indicates the portion of information in the imaginary part. For 300-nm PS, it is about 20% for the polarizability, and is negligible for the Rytov field (about 0.3%). Moreover, the amount of crosstalk in the polarizability imaginary part depends on the particle size and it is thus non-trivial to retrieve the actual refractive index as compared to our Rytov approach.

S5 Size evaluation from tracking

Even following a random motion in the solution, NP movement obeys a statistical law, where its average displacement depends on the NP size. Therefore, the nanoparticle tracking analysis (NTA) enables NP size evaluation.

If the tracking is carried out in N_d dimensions, and it consists of N positions which is separated by a stable time lag of Δt, the mean square displacement (MSD) is expressed as :

$$< \Delta r^2 >= \frac{\sum_{i=1}^{N} (r_{i+1} - r_i)^2}{N} = 2\, N_d\, D\, \Delta t \tag{S12}$$

, where r_i and r_{i+1} are the NP positions in two consecutive images. The diffusion coefficient D is described by the Stokes - Einstein equation allowing the NP size evaluation:

$$D = \frac{k_B T}{3\pi\, \eta\, d_{NP}} = \frac{< \Delta r^2 >}{2\, N_d\, \Delta t} \quad \Leftrightarrow \quad d_{NP} = \frac{k_B T}{3\pi\, \eta} \cdot \frac{2\, N_d\, \Delta t}{< \Delta r^2 >} \tag{S13}$$

, where, k_B is the Boltzmann constant, T the temperature, and η the dynamic viscosity of the solution.

This method of NP size evaluation is slowly converging when increasing the number of position along the trace (logarithmic convergence) [10]. In our experiment, the tracking is carried out mostly around 20-50 positions, specially for the biological sample which interacts weakly with light (**Fig S3**). Therefore, the size determination presents an important error which lower other physical measurement precision.

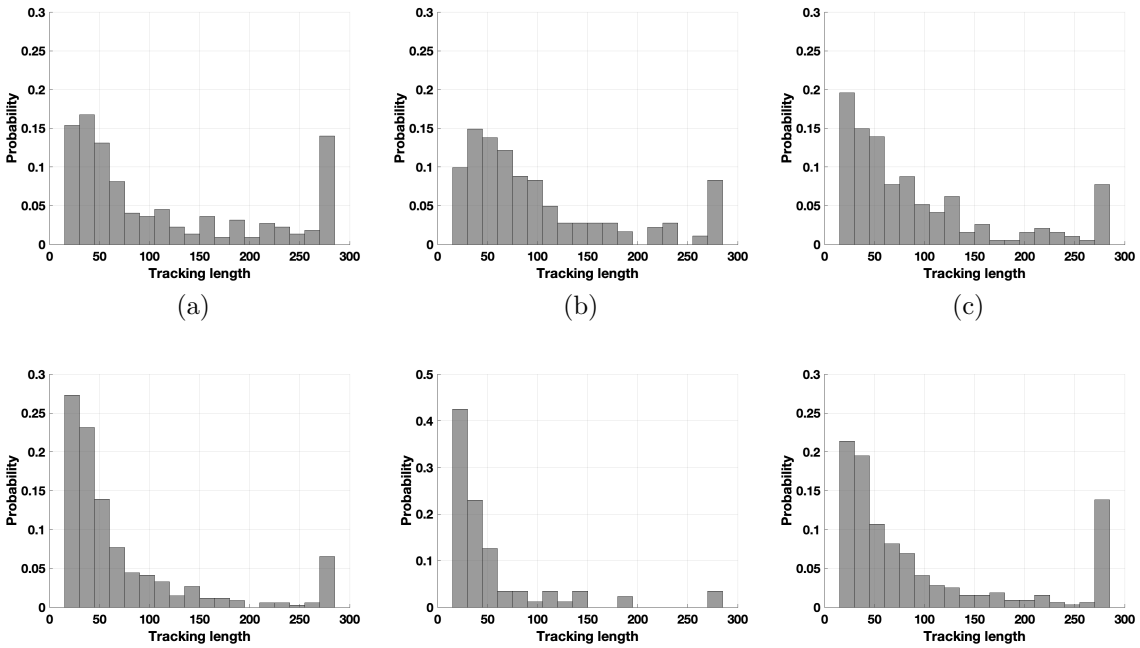

Figure S3: **Distribution of tracking length for different samples**. **(a)** 100-nm PS, **(b)** 200-nm PS, **(c)** 100-nm Au, **(d)** HIV-1 WT, **(e)** SARS-CoV-2, **(f)** Extracellular vesicles.

In order to improve the size determination, each NP's size is evaluated by taking into account the tracks of other NPs with a weighting coefficient. We use our unique technique to establish this weight coefficient as the correlation of between two Rytov DAI images, as introduced in our recent paper [11].

The movement of i^{th} NP is split equally by parity into two tracks. The difference between two respective calculated DAI images infers the intrinsic error σ_i^2 of the NP's tracking, expressed by the signal variance. Between i^{th} and k^{th} NPs, their interrelated error $\sigma_{i,k}^2$ is defined by the same methods, but using two DAI images. The fraction $\sigma_{i,k}^2/\sigma_i^2$ carries the difference between two NPs : it increases when the similarity increases, and tends to 1 if the two particles are identical. Size of i^{th} NP is determined by a linear fit between MSD and time lags of all the NPs with the weight coefficient of $(\sigma_i^2/\sigma_{i,k}^2)^{n_w}$. The exponent n_w is chosen experimentally so that it is neither too important to homogenize different NPs, nor too weak to effectively narrow down the measurement.

In order to determine the optimal exponent, simulated study is carried out for a batch of 100-nm PS NPs, each NP tracks (200 positions) are generated numerically satisfying the stochastic law. We define the relative size error as the absolute difference between measured size versus real size, normalized by real size. For the classical NTA, the relative size error is $\approx 12\%$. At the optimal exponent $n_w = 1.125$ for weighted NTA, the relative size error is about 3%, proving a 4-fold gain in size precision, as illustrated in **Figure S4a**.

Figure S4b shows the difference between the size evaluation of monodisperse 100-nm PS, with and without the weighting process. The standard deviation of measurement is reduced (by a factor of 2), whereas the average value remains almost constant.

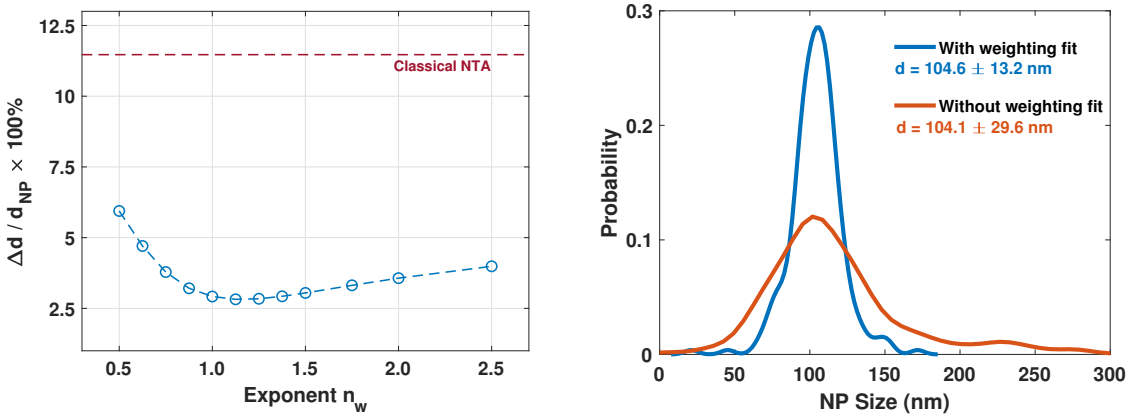

(a) (b)

Figure S4: **Size evaluation from tracking**. **(a)** Simulation of Rytov-based weighted nanoparticle tracking a nalysis for solution of 100-nm PS NP. Relative size error is reduced from 12% (in case of classical NTA) to 3% (at the optimal exponent). **(b)** Size determination of a monodisperse 100-nm PS, with and without weighting fit.

S6 Depth of Field of different particles

Depth of Field of View (FoV) is estimated from the number of detected particles while varying the volume of numerical propagation. The number of detected particles should be stable after reaching a certain threshold, linked to the particle signal to noise ratio on the phase and intensity images. This is where we define the depth of FoV. Particle number is statistically increasing when the propagation is carried beyond this threshold. It may be explained by the introduction of artifacts or image border's effect. An example of 100-nm PS solution is illustrated in **Figure S5a**. Multiple images are taken into accounts, and its average number of particles is shown as red line, approving the estimation of depth of FoV of about 25-μm.

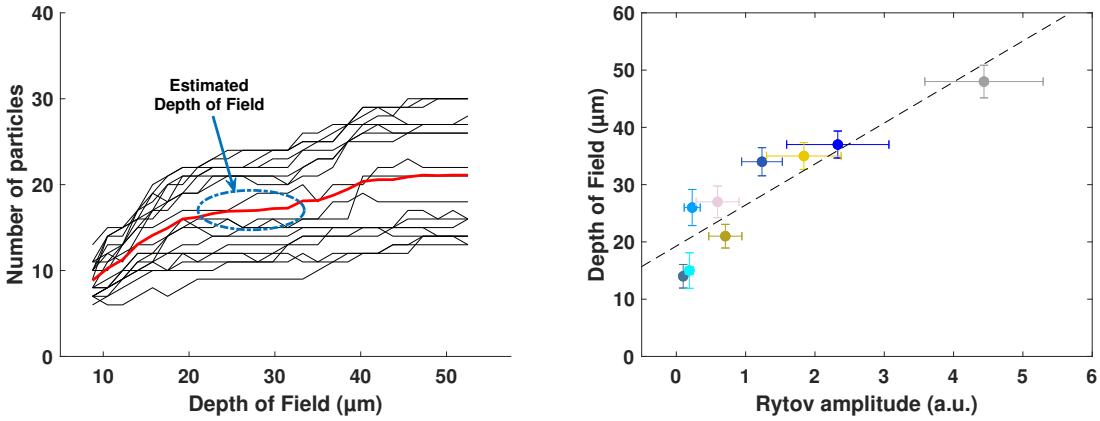

(a) (b)

Figure S5: **(a)** Analysis of the depth of FoV of 100nm PS. **(b)** Depth of FoV in function of Rytov amplitude for various particles (color-coded nature of particle, cf main text).

Figure S5b shows depth of FoV for different types of particles in function of their Rytov intensities. Its linearity grants access to the depth of FoV without any *a priori* knowledge of particle, since Rytov intensities can easily be determined from acquired images.

S7 Deep Learning training procedure

For the training, data cleaning has been performed based on 2 criteria: the quality of particle tracking and image averaging. For the monodisperse solution, we defined a confident interval as 3 times the standard deviation. If the NP size is determined outside this interval, the particle is considered as an outlier and is removed from the training data set. Moreover, as border effects are perturbing image averaging, particles located close to the edges of the holographic volume are also removed from the training set. A process of data augmentation is applied in order to increase the model stability and to avoid the over-fitting bias for a class containing numerous individual NPs as compared to some others [12, 13]. In total, the data set is composed of 2145 NPs after cleaning and data augmentation (195 per class). Thanks to the radial symmetries and the absence of shift problems, our neural network had less difficulties to learn with a small data set. We increase its performance by adding a bagging method, 80 models are trained with 80 sub-dataset (random sampling with replacement) in order to reduce full dataset variability bias.

Figure S6a illustrates the average loss function (cross-entropy) evolution versus epochs. The evolution indicates that our training procedure does not present over- or under-fitting.

In the main text, the confusion matrices are shown for all the classes or just for the 3 main categories (dielectric, metallic or biological nanoparticle). The gain in reducing the number of class is negligible. Indeed, reducing the number of class -by pooling in one class all the biological objects on the one hand (Fig S6b) or the inert particles on the other hand (Fig S6c)- does not lead to a significant improvement of classification quality. Of course, in the each pooled class the precision is increasing in absolute since all the error in classification between particles within the pooled class is not anymore a mis-classification.

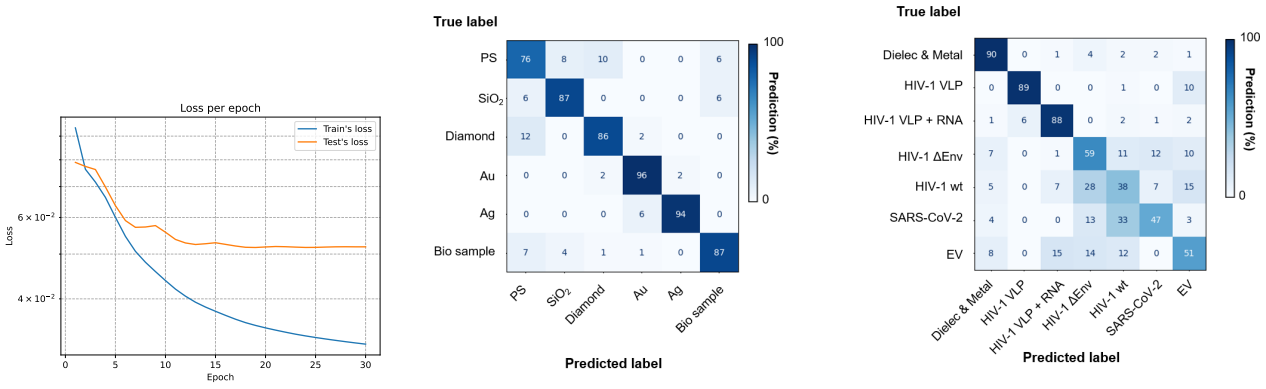

(a) (b) (c)

Figure S6: (a) Loss function evolution for training data and test data. (b, c) Confusion matrix for two training model which identifies more precisely either dielectric and metal particle (b), or biological particles (c).

S8 Coefficient for the dry mass determination of virus

It was shown that the integration of optical path difference is proportional to the dry mass of cells [3, 4].

$$\iint \Delta\ell \cdot dx\, dy \;=\; \alpha \cdot m \quad : \text{where } \alpha = 0.18\,\mu m^3\, pg^{-1} \text{ for most of the eukaryotic cells}$$

This expression is equivalent to our Re(SIR), except the coefficient is actually changed by a factor of $2\,n_m$ (see equation (S6)). On the other hand, the coefficient $\alpha = 0.18\,\mu m^3/pg$ (or equivalent to $\beta_{SIR} = 2.08\,pg \cdot \mu m^{-3}$) is incorrect to estimate the virus mass, because of the difference of refractive index between virus and eukaryotic cells. Indeed, the refractive index of a eukaryotic cell is basically the same with the cytosol ($n_{cyto} = 1.360 - 1.390$ [14]), which consist of the majority of the cell. However, the proportion of genetic material is more important in the case of virus. Indeed, the refractive index of viruses are mostly between $1.4 - 1.6$ [15], inducing a smaller coefficient β_{SIR} which is proportional to $(n - n_m)$ (see equation S6). Therefore, the estimation of refractive index for each virus has an important influence for the determination of its dry mass. We introduce our method to estimate the refractive index of virus from its size : a first approach bases on the Maxwell-Garnett effective refractive index, and then a second approach bases on a direct logarithmic fitting of literature values.

In the first approach (Maxwell-Garnett), virus spikes (glycoproteins and envelope proteins) are not taken into account for the estimation of virus's refractive index for two reasons. First, the literature usually measures virus size by electronic microscope, therefore the indicated size is mostly the virus capsid. Second, even though the spikes contribute to hydrodynamics size, their dry volume proportion are small, especially for large viruses. Hence, their contribution in refractive index can be neglected to determine our first naive refractive index versus size law.

We consider that the virus capsid (refractive index n_{vi} and volume V_{vi}) consist of two main parts : biological material (n_G and V_G) and inside medium (n_i and V_i). Given the outside medium can be -optical speaking- considered as pure water, the effective refractive index of the virus $\tilde{n}_{vi}$ is:

$$\tilde{n}_{vi}^2 = \frac{n_{vi}^2 - n_m^2}{n_{vi}^2 + 2\,n_m^2} = \underbrace{\frac{n_G^2 - n_m^2}{n_G^2 + 2\,n_m^2}}_{\tilde{n}_G^2}\,\frac{V_G}{V_{vi}} + \underbrace{\frac{n_i^2 - n_m^2}{n_i^2 + 2\,n_m^2}}_{\tilde{n}_i^2}\left(1 - \frac{V_G}{V_{vi}}\right), \tag{S14}$$

where $\tilde{n}_G$ and $\tilde{n}_i$ effective refractive index of the biological material and the inside medium respectively. Assuming at the first order that the volume of biological material is similar for all the virus, the equation (S14) can be written as :

$$V_G = V_{vi} \cdot \frac{\tilde{n}_{vi}^2 - \tilde{n}_i^2}{\tilde{n}_G^2 - \tilde{n}_i^2} = cte \Longleftrightarrow \left(\tilde{n}_{vi}^2 - \tilde{n}_i^2\right) V_{vi} = cte = A \Longleftrightarrow \tilde{n}_{vi}^2 = \tilde{n}_i^2 + \frac{A}{V_{vi}}. \tag{S15}$$

The effective refractive index of virus is therefore proportional to $1/V_{vi}$. Using the measured values of refractive index of various virus and extracellular vesicles [15, 16], the linear regression coefficients are determined as $A = 2.196 \times 10^{-5}\ \mu m^3$ and $\tilde{n}_i^2 = 0.031$ (graph shown is **Fig S7**). The refractive index of virus capsid having diameter of D can be deduced:

$$n_{vi} = n_m \sqrt{\frac{2\,\tilde{n}_{vi}^2 + 1}{1 - \tilde{n}_{vi}^2}} \quad \textbf{where} \quad \tilde{n}_{vi}^2 = \frac{6\,A}{\pi\,D^3} + \tilde{n}_i^2. \tag{S16}$$

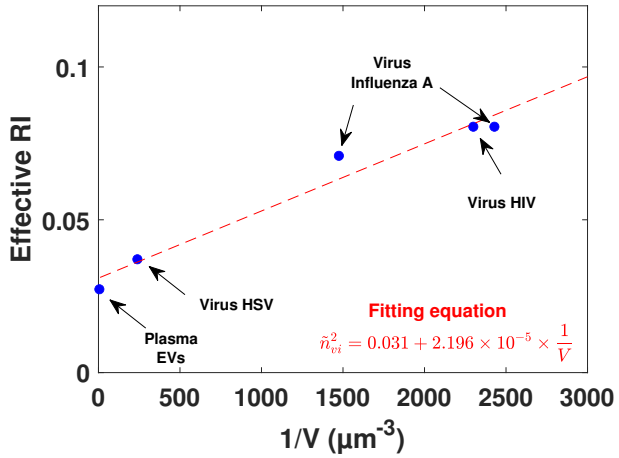

Figure S7: Relation between the effective refractive index and the volume of virus. Data using the information of several virus from [15, 16]

Finally, for a virus capsid having diameter of D (or virus' hydrodynamics size of $D + \ell_h$), its mass is determined by :

$$m = \frac{1}{2\, n_m\, \alpha}\, \frac{n_{cyto} - n_m}{n_{vi} - n_m} \cdot \mathrm{Re(SIR)} \tag{S17}$$

, where $\alpha = 0.18\, \mu m^3/pg \approx 3 \times 10^{-7} \mu m^3/\mathrm{MDa}$ is the coefficient mentioned above for eukaryotic cells.

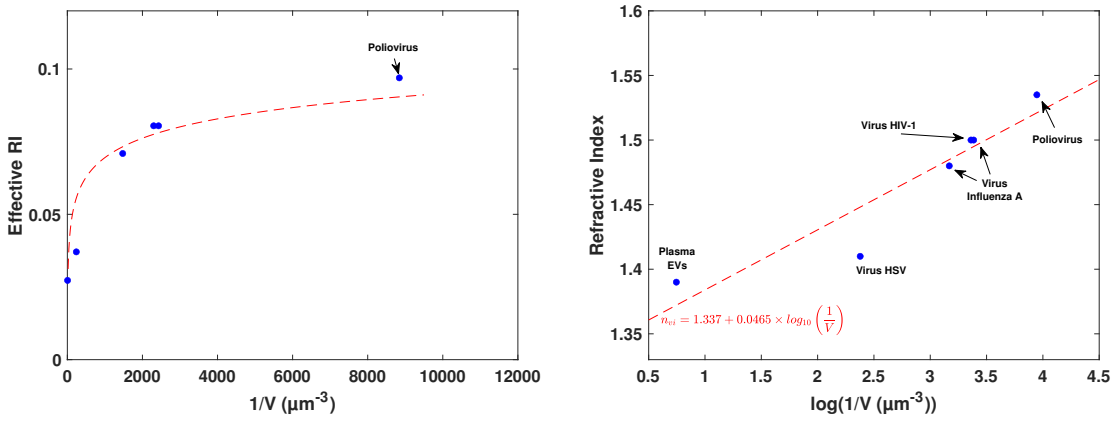

(a) (b)

Figure S8: **(a)** Effective refractive index in function the reciprocal of virus volume. The red dash line illustrates the fitting equation in our model. Smaller virus (poliovirus) does not follow the hypothesis . **(b)** Refractive index in function of logarithm of the reciprocal of virus volume. The dash lines illustrate the linear fit : red one is for all the virus and plasma EVs, blue one is for virus only.

However, the strong hypothesis of similar biological material volume for all the virus used to make a first order development from the Maxwell-Garnett calculation reaches its limits for smaller than 100-nm viruses (like poliovirus having diameter of 60-nm, refractive index of 1.535 [17] or a priori SARS-CoV-2). Indeed, fig. S8a we see a clear logarithmic dependency of the

effective refractive index (confirmed for the real refractive index in fig. S8b) with the reciprocal of virus volume. We deduce a second order law to directly fit the refractive index of biological nanoparticles as a function of its diameter d (in μm):

$$n_{vi} = 1.337 + 0.0465 \times \log_{10}\left(\frac{6}{\pi\, d^3}\right) \tag{S18}$$

The difference in dry mass determination is shown in the following table.

	Dry Mass (MDa)	
	Maxwell-Garnett calculation	Logarithm fitting
HIV-1 VLP	57^{+15}_{-17}	52^{+13}_{-15}
HIV-1 VLP + RNA	131^{+54}_{-32}	111^{+46}_{-27}
HIV-1 wt	108^{+40}_{-29}	92^{+34}_{-24}
HIV-1 ΔEnv	68^{+24}_{-27}	64^{+22}_{-16}
SARS-CoV-2	18^{+6}_{-7}	31^{+10}_{-13}
Extracellular vesicles	262^{+130}_{-114}	227^{+112}_{-98}

We remark that the values are slightly different within the confident range for all the biological samples, except for SARS-CoV-2. It may be explained by its small size which is not suitable for our simple model of Maxwell-Garnett approximation, with a non-negligeable contribution from the protein spikes. Therefore, in the paper, we exhibit the results from logarithmic fit to better take into account the whole particle composition.

S9 Comparison of estimated dry mass of virus

In the main text, we have discussed the determination of dry mass of virus from the measurement of Rytov field. In order to verify the experimental value, we compare it to the dry mass estimated from the virus molecular compositions.

Virus HIV-1

HIV-1 composition can found in the literature [18, 19] as: 2 single-stranded RNA (≈10 kilobases each), ∼1200 copies of p55 Gag (55 kDa each, the capsid shell being assembled from ∼1200 copies of Cap24), ∼60 copies of p160 Gag-Pol (160 kDa each) and 6 to 20 $Gp160^{Env}$ trimers (220 kDa each monomer, taking into account ∼25 glycosylation sites of ∼2.5 kDa each) . This provides 6.6 MDa (RNA) + 66 MDa (structural proteins) + 10 to 16 MDa (enzymes) + 4 to 13 MDa for Env. The molecular mass of a particle should lie within a range of 90 to 102 MDa without including its lipid membrane, small accessory proteins (Vpr, Vif) and cellular components (tRNA) which are negligible in the total mass. This is in excellent agreement with our measurement (≈ 92 MDa).

Virus SARS-CoV-2

For SARS-CoV-2, the literature remains incomplete, making mass estimation highly hypothetical with current knowledge. In addition, the content of viral particles appears highly variable, with particles more or less rich in N, M and S. A 'typical' viral particle would contain RNA genomes of 30-kilobases (∼10MDa) bound to 700-1000 N protein units (50kDa each), 1000 M protein dimers (25kDa each) and 25 to 100 S proteins (76kDa) [20, 21]. A very rough estimate would give a molecular weight of between 72MDa and 93MDa, beyond our measurements (≈ 31 MDa).

This difference could have multiple reasons. First, it may be explained by the presence of a mixture of more or less filled viral particles, more or less decorated with Spikes. Importantly, measurements on HIV-1 and derivatives were carried out on particles purified by calibrated methods, enabling most of the EVs to be removed. This was not the case with SARS-CoV-2, whose purification at high concentration and separation from EVs are not established yet. Thus, the SARS-CoV-2 samples used here were issued from cell supernatant and highly enriched in EVs, which could have influenced our results.

Second, our method of dry mass determination bases on a hypothesis that the virus is transparent (without any light absorption). However, it may not be the case for SARS-CoV-2. We observe a slight absorption via the analysis of intensity and phase images. Moreover, our model for the estimation of virus refractive index is simple and naive, based on the hypothesis that all the virus have comparable structure. Indeed, due to the lack of researches on virus refractive index, we fit our model with several points. Since SARS-CoV-2 has a highly dense structure (almost the same mass of HIV-1, but 7 times smaller in volume), our model may over-estimate its refractive index, provoking to the under-estimation of its dry mass.

Extracellular vesicles

In this publication, we calculate the extracellular vesicles (EVs) dry mass considering the law determined with viruses, linking the particle refractive index with its size. However, it is not an accurate assumption since EVs are mainly hollow compared to viruses. The refractive index of EVs might be quite independent to its size with a value close to the cytoplasma refractive index and not the value of up to 1.50 for the small size when considering or law.

If the sample can be identified as EVs (by *a priori* knowledge or by machine learning), we can applied the coefficient equivalent to that of cell (2.08 $pg \cdot \mu m^{-3}$). That modifies the EVs dry mass to 433^{+214}_{-188} MDa, about 200% error compared to the value of 227^{+112}_{-98} MDa in the main text.

References

[1] Y. Cotte, F. Toy, P. Jourdain, N. Pavillon, D. Boss, P. Magistretti, P. Marquet, C. Depeursinge, Marker-free phase nanoscopy, *Nature Photonics* **7**, 113–117 (2013).

[2] P. Bon, S. Aknoun, S. Monneret, B. Wattellier, Enhanced 3D spatial resolution in quantitative phase microscopy using spatially incoherent illumination, *Opt. Express* **22**, 8654 (2014).

[3] R. Barer, Interference microscopy and mass determination, *Nature* **169**, 366 (1952).

[4] S. Aknoun, J. Savatier, P. Bon, F. Galland, L. Abdeladim, B. F. Wattellier, S. Monneret, Living cell dry mass measurement using quantitative phase imaging with quadriwave lateral shearing interferometry: an accuracy and sensitivity discussion, *J Biomed Opt.* **20**, 126009 (2015).

[5] H. Sierra, C. A. DiMarzio, D. H. Brooks, Modeling phase microscopy of transparent three-dimensional objects: a product-of-convolutions approach, *JOSA A* **26**, 1268 (2009).

[6] P. Bon, B. Wattellier, S. Monneret, Modeling quantitative phase image formation under tilted illuminations, *Opt. Lett.* **37**, 1718 (2012).

[7] X. Michalet, Mean square displacement analysis of single-particle trajectories with localization error: Brownian motion in an isotropic medium, *Physical Review E* **82**, 041914 (2010).

[8] S. Khadir, D. Andrén, P. C. Chaumet, S. Monneret, N. Bonod, M. Käll, A. Sentenac, G. Baffou, Full optical characterization of single nanoparticles using quantitative phase imaging, *Optica* **7**, 243 (2020).

[9] X. Zhang, J. Qiu, X. Li, J. Zhao, L. Liu, Complex refractive indices measurements of polymers in visible and near-infrared bands, *Appl. Opt.* **59**, 2337 (2020).

[10] H. Qian, M. Sheetz, E. Elson, Single particle tracking. analysis of diffusion and flow in two-dimensional systems, *Biophysical Journal* **60**, 910 (1991).

[11] M.-C. Nguyen, P. Bon, Optical signal-based improvement of individual nanoparticle tracking analysis, *Measurement Science and Technology* **35**, 015202 (2024).

[12] A. Mikołajczyk, M. Grochowski, *2018 International Interdisciplinary PhD Workshop (IIPhDW)* (2018), pp. 117–122.

[13] X. Li, W. Zhang, Q. Ding, Cross-domain fault diagnosis of rolling element bearings using deep generative neural networks, *IEEE Transactions on Industrial Electronics* **66**, 5525 (2019).

[14] W. Choi, C. Fang-Yen, K. Badizadegan, N. L. Seungeun Oh, R. R. Dasari, M. S. Feld, Tomographic phase microscopy, *Nature Methods* **4**, 717 (2007).

[15] Y. Pang, H. Song, W. Cheng, Using optical trap to measure the refractive index of a single animal virus in culture fluid with high precision, *Biomed. Opt. Express* **7**, 1672 (2016).

[16] A. I. Konokhova, M. A. Yurkin, A. E. Moskalensky, A. V. Chernyshev, V. P. Maltsev, E. D. Chikova, G. A. Tsvetovskaya, Light-scattering flow cytometry for identification and characterization of blood microparticles, *Journal of Biomedical Optics* **17**, 057006 (2012).

[17] R. L. Steere, F. L. Schaffer, The structure of crystals of purified mahoney poliovirus, *Biochimica et Biophysica Acta* **28**, 241 (1958).

[18] J. R. Perilla, K. Schulten, Physical properties of the HIV-1 capsid from all-atom molecular dynamics simulations, *Nature Communications* **8** (2017).

[19] E. O. Freed, HIV-1 assembly, release and maturation, *Nature Reviews Microbiology* **13** (2015).

[20] W. Pezeshkian, F. Grünewald, O. Narykov, S. Lu, V. Arkhipova, A. Solodovnikov, T. A. Wassenaar, S. J. Marrink, D. Korkin, Molecular architecture and dynamics of sars-cov-2 envelope by integrative modeling, *Structure* **31**, 492 (2023).

[21] B. W. Neuman, G. Kiss, A. H. Kunding, D. Bhella, M. F. Baksh, S. Connelly, B. Droese, J. P. Klaus, S. Makino, S. G. Sawicki, S. G. Siddell, D. G. Stamou, I. A. Wilson, P. Kuhn, M. J. Buchmeier, A structural analysis of m protein in coronavirus assembly and morphology, *Journal of Structural Biology* **174**, 11 (2011).